

Detecting strongly lensed supernovae at $z \sim 5 - 7$ with LSST

Claes-Erik Rydberg^{1*}, Daniel J. Whalen², Matteo Maturi¹, Thomas Collett²,
Mauricio Carrasco¹, Mattis Magg¹, Ralf S. Klessen^{1,3}

¹*Universität Heidelberg, Zentrum für Astronomie, Institut für Theoretische Astrophysik, Albert-Ueberly-Str. 2, 69120 Heidelberg, Germany*

²*Institute of Cosmology and Gravitation, University of Portsmouth, Dennis Sciama Building, Portsmouth PO1 3FX, UK*

³*Universität Heidelberg, Interdisziplinäres Zentrum für Wissenschaftliches Rechnen (IWR), 69120 Heidelberg, Germany*

Accepted XXX. Received YYY; in original form ZZZ

ABSTRACT

Supernovae (SNe) could be powerful probes of the properties of stars and galaxies at high redshifts in future surveys. Wide fields and longer exposure times are required to offset diminishing star formation rates and lower fluxes to detect useful numbers of events at high redshift. In principle, the Large Synoptic Survey Telescope (LSST) could discover large numbers of early SNe because of its wide fields but only at lower redshifts because of its AB mag 24 - 25 limits. But gravitational lensing by galaxy clusters and massive galaxies could boost flux from ancient SNe and allow LSST to detect them at earlier times. Here, we calculate detection rates for lensed SNe at $z \sim 5 - 7$ for LSST. We find that the LSST main survey could detect $\sim 1 - 2$ lensed Population III (Pop III) SN but 130-1400 Pop I/II SNe. An alternative deep survey with a one-year cadence could find ~ 10 Pop III SNe with an 84h exposure and ~ 50 SNe with a 420h exposure.

Key words:

gravitational lensing; strong – stars: Population III – galaxies: high-redshift – cosmology: observations – cosmology: dark ages, reionization, first stars: early universe – supernovae: general

1 INTRODUCTION

High redshift SNe are powerful probes of the properties of stars and their formation rates at early times because they can be observed at great distances and, to some degree, the masses of their progenitors can be inferred from their light curves. Early SNe could complement gamma-ray bursts (GRBs) as tracers of stellar populations in the first galaxies (Robertson & Ellis 2012; see also Johnson et al. 2009; Greif et al. 2010; Pawlik et al. 2011; Jeon et al. 2012; Wise et al. 2012; Pawlik et al. 2013; Muratov et al. 2013; Xu et al. 2013; O’Shea et al. 2015). They can also constrain scenarios for early cosmological reionization (e.g., Whalen et al. 2004; Kitayama et al. 2004; O’Shea et al. 2005; Susa & Umemura 2006; Alvarez et al. 2006; Abel et al. 2007; Whalen et al. 2008a; Susa et al. 2009; Whalen et al. 2010) and early chemical enrichment (Mackey et al. 2003; Bromm et al. 2003; Kitayama & Yoshida 2005; Smith & Sigurdsson 2007; Greif et al. 2007; Whalen et al. 2008b; Smith et al. 2009; Joggerst

et al. 2010; Greif et al. 2010; Safranek-Shrader et al. 2014; Smith et al. 2015; Ritter et al. 2016; Sluder et al. 2016; Chen et al. 2017a,b; Hartwig et al. 2018).

In principle, detections of SNe at $z \gtrsim 20$ could even reveal the properties and formation rates of Population III (Pop III) stars at cosmic dawn (Moriya et al. 2010; Tominaga et al. 2011; Tanaka et al. 2012; Hummel et al. 2012; Tanaka et al. 2013; de Souza et al. 2013, 2014) and shed light on the origins of supermassive black holes (SMBHs; Alvarez et al. 2009; Whalen & Fryer 2012; Johnson et al. 2012, 2013a; Hosokawa et al. 2013; Johnson et al. 2014; Umeda et al. 2016; Woods et al. 2017; Smidt et al. 2017; Haemmerlé et al. 2018a,b). Primordial SNe will impose one of the few direct constraints on the Pop III initial mass function (IMF) in the near term because the stars themselves will not be visible to the *James Webb Space Telescope* (JWST; Gardner et al. 2006; Rydberg et al. 2013) or to 30 - 40 m telescopes on the ground, and because numerical simulations cannot predict their properties from first principles (e.g., Bromm et al. 2009; Bromm & Yoshida 2011; Whalen 2013; Glover 2013).

Longer exposure times and larger survey areas are re-

* E-mail: mail@utte.nu

quired to detect transients at high redshifts because of their lower luminosities and smaller star formation rates (SFRs) at early epochs. *JWST* and the ELTs will have the sensitivity required to detect even the earliest explosions but only in narrow fields of view that may not capture many events (Hartwig et al. 2017 predict about 1 SN per year). On the other hand, LSST (Ivezic et al. 2008), *Euclid* (Laureijs et al. 2011) and the Wide-Field Infrared Survey Telescope (*WFIRST*; Spergel et al. 2015) could harvest far greater numbers of events because of their large survey areas but only at lower redshifts because of their lower sensitivities. Furthermore, because LSST is limited to the *Y* band in wavelength it cannot detect transients above $z \sim 6 - 7$, and because *Euclid* and *WFIRST* are limited to the *H* band they cannot detect SNe at $z \gtrsim 13 - 14$. This is due to the fact that flux blueward of the Lyman- α wavelength in the source frame of an event at $z > 6$ is absorbed by the neutral intergalactic medium (IGM) prior to the end of cosmological reionization. The optimum bands for detecting SNe at $z \sim 20$ are in the near infrared (NIR) at 2 - 5 μm (Whalen et al. 2013b,c,g).

But gravitational lensing by galaxy clusters and massive galaxies could offset the lower sensitivities of wide-area surveys and reveal more transients than would otherwise be detected. Strongly lensed SNe at $z \sim 1 - 2$ (Amanullah et al. 2011; Kelly et al. 2014; Schmidt et al. 2014) and lensed protogalaxies at $z \gtrsim 6$ (e.g. Zheng et al. 2012; Coe et al. 2013; Bradley et al. 2014; Vanzella et al. 2014; Rydberg et al. 2015, 2017) have already been found in studies of individual, well-resolved cluster lenses. Recent studies suggest that such surveys could detect SNe at even higher redshifts ($z \gtrsim 10$; Pan et al. 2012; Whalen et al. 2013a). Oguri & Marshall (2010) calculated the number of lensed SNe that might be found by LSST at $z < 3.75$, and Goldstein & Nugent (2017) explain how this number could be increased by an order of magnitude.

In this paper we estimate the number of a variety of strongly-lensed SNe that could be found by LSST at $z \lesssim 7$. Although LSST optical bands limit SN detections to this redshift, they could constrain cosmic SFRs at the epoch of reionization, and a few of them might even be Pop III SNe, given that numerical simulations predict the formation of zero-metallicity stars down to $z \sim 3$ (Trenti et al. 2009) and large parcels of pristine gas have now been discovered at $z \sim 2$ (Fumagalli et al. 2011). Lensed supernovae of any type at these redshifts may also be interesting as probes of the cosmic expansion history (Foxley-Marrable et al. 2018). In Section 2 we discuss our SN spectra and explosion rates. We also describe how magnification maps are calculated for large fields and combined with redshifted spectra in specific filters to obtain SN detection rates. Event rates for the LSST main survey and a proposed deep survey optimized to detect Pop III explosions are examined in Section 3 and we conclude in Section 4.

2 METHOD

We convolve cosmic SN rates (SNRs) as a function of redshift with spectra from radiation hydrodynamical simulations, new magnification maps for wide fields and LSST filter response functions to predict detection rates

for a variety of lensed SNe. We assume Λ CDM cosmological parameters from the first-year *Planck* best fit lowP+lensing+BAO+JLA+H₀: $H_0 = 67.3$, $\Omega_M = 0.308$, and $\Omega_\Lambda = 0.692$ (Planck Collaboration et al. 2014). We have verified that these parameters yield SN detection rates that are essentially identical to those obtained with the more recent Planck Collaboration et al. (2016) parameters.

2.1 SN Spectra

We use Pop III SNe as proxies for explosions at all metallicities for simplicity. At $z \sim 5 - 7$ most stars will be enriched to some degree, but the computational costs of a grid of spectra in both progenitor mass and metallicity would be prohibitive. Furthermore, the average global metallicities one would assign to stars at any given redshift in this range are not yet known. Although 10 - 30 M_\odot Pop III stars are expected to be hotter and more compact than Pop II/I stars of equal mass because of their lower internal opacities (Tumlinson et al. 2001), they are expected to explode with similar energies and luminosities (see Chieffi & Limongi 2004; Woosley & Heger 2007 and Figure 1 of Whalen & Fryer 2012). However, the use of Pop III CC SNe as substitutes for Pop II/I explosions could cause us to underestimate their rest frame luminosities, as *U*, *B*, *V*, *R* and *I* band light curves for our 15 M_\odot 1.2 foe RSG explosion are about ten times dimmer than those for the M15_E1.2_Z1 model in Kasen & Woosley (2009) (1 foe = 10^{51} erg; see Figure 7). We therefore also calculate, as an upper limiting case, LSST detection rates assuming our CC SN spectra to be a factor 10 brighter.

2.1.1 Final Fates of Pop III Stars

Non-rotating 8 - 30 M_\odot Pop III stars die as core-collapse (CC) SNe and 140 - 260 M_\odot stars explode as pair-instability (PI) SNe (Heger & Woosley 2002; see also Rakavy & Shaviv 1967; Barkat et al. 1967; Joggerst & Whalen 2011; Chen et al. 2014c). 30 - 90 M_\odot stars collapse to BHs unless they are very rapidly rotating, in which case they can produce a gamma-ray burst (GRB; e.g., Gou et al. 2004; Yoon & Langer 2005; Bromm & Loeb 2006; Whalen et al. 2008c; Mesler et al. 2012, 2014) or a hypernova (HN; Nomoto et al. 2010). Stars more massive than 260 M_\odot encounter the photodisintegration instability and collapse to BHs, but at very high masses ($\gtrsim 50\,000 M_\odot$) a few stars may die as extremely energetic SNe due to the general relativistic instability (Monterio et al. 2012; Johnson et al. 2013b; Whalen et al. 2013e,f,h; Chen et al. 2014a).

Pop III stars can actually encounter the PI at masses as low as $\sim 100 M_\odot$, but below 140 M_\odot it triggers the ejection of multiple, massive shells rather than the complete destruction of the star. Collisions between these shells can then produce very bright events in the UV (pulsational PI (PPI) SNe; Woosley et al. 2007; Cooke et al. 2012; Chatzopoulos & Wheeler 2012b; Chen et al. 2014b). Rotation can cause stars to explode as PI SNe at masses as low as $\sim 85 M_\odot$ (rotational PI (RPI) SNe; Chatzopoulos & Wheeler 2012a; Chatzopoulos et al. 2013 – see also Yoon et al. 2012). Very massive Pop II/I stars with metallicities below $\sim 0.3 Z_\odot$ can retain enough mass to die as PI SNe (Langer et al. 2007; Whalen et al. 2014b; Kozyreva et al. 2014b). 10 - 30 M_\odot

stars can also eject shells prior to explosion, and the collision of the ejecta with the shell can, like PPI SNe, produce highly luminous events that are brighter than the explosion itself (Type IIn SNe).

In our study we include spectra for 150, 175, 200, 225 and 250 M_{\odot} Pop III PI SNe (Whalen et al. 2013b,g; see Kasen et al. 2011; Dessart et al. 2013; Kozyreva et al. 2014a; Jerkstrand et al. 2016 for other PI SN spectra and light curves). We also have spectra for 15 and 25 M_{\odot} Pop III CC SNe (Whalen et al. 2013c), each of which can have explosion energies of 0.6, 1.2 or 2.4 foe with equal probability. The structure of the star at death can have a profound effect on the light curve of the explosion but is not well constrained by 1D evolution models, so we consider explosions of both compact blue supergiants (BSGs) and red supergiants (RSGs) at each mass to bracket the range of spectra expected for CC and PI SNe. Consistent with the numbers of Type IIP SNe observed today, we take 75% of the stars to die as RSGs.

We also include spectra for 40 M_{\odot} Pop III Type IIn SNe (Whalen et al. 2013d), assuming that 1% of all CC SNe produce shell collisions, but ignore GRBs and HNe because of their small numbers ($\lesssim 10^{-3}$ of all CC events). Our grid of models also has spectra for 90 - 140 M_{\odot} RPI SNe at 5 M_{\odot} increments, which are essentially the explosions of stripped He cores (Smidt et al. 2015; see Chatzopoulos et al. 2015 for additional spectra). A 110 M_{\odot} PPI SN is also included (Whalen et al. 2014a). More or less massive PPI progenitors either do not produce collisions that are bright in the visible/NIR today or shells that collide at all. Since this mass falls in the same range as RPI SNe we assume that 50% of the stars from 107.5 - 112.5 M_{\odot} die as PPI SNe.

Primordial stars are not thought to lose much mass over their lives because of their low internal opacities, which prevent strong winds (Baraffe et al. 2001; Kudritzki 2000; Vink et al. 2001; Ekström et al. 2008). Consequently, their explosion rates can be derived directly from their SFRs and IMF because their masses at death are nearly those at birth. But mass loss in Pop I and II stars can place some of them into mass ranges in which they will explode at the end of their lives while removing others. This introduces some ambiguity into their explosion rates because mass loss rates are not well constrained by either stellar mass or metallicity. For simplicity, we make no attempt to account for mass loss in our Pop II/I SNRs and just apply the same mass ranges for Pop III SNe to them.

2.1.2 Spectrum Models

Our spectra were calculated in three stages. First, the progenitor star was evolved from birth to the onset of collapse and explosion in Kepler (Weaver et al. 1978; Woosley et al. 2002) or GENEVA (Eggenberger et al. 2008; Haemmerlé et al. 2013, 2016), which are one-dimensional (1D) Lagrangian stellar evolution codes. After all explosive burning was complete (typically in 10 - 30 sec) the shock, surrounding star, and its envelope were mapped onto a 1D Eulerian grid in the radiation hydrodynamics code RAGE (Gittings et al. 2008) and evolved for 6 months to 3 years, depending on explosion type. Blast profiles from RAGE were then post processed with the SPECTRUM code (Frey et al. 2013) to obtain source frame spectra for the fireball at every stage of its evolution.

Flux-limited diffusion (FLD) with gray OPLIB opacities (Magee et al. 1995) in RAGE were used to transport radiation through the SN ejecta, but monochromatic OPLIB opacities were used in SPECTRUM to produce spectra with 13899 wavelengths from hard X-rays down to the far IR. Gray FLD enables RAGE to properly capture shock breakout from the star and the expansion of the ejecta into the IGM while monochromatic opacities allow SPECTRUM to synthesize emission and absorption lines from the fireball in addition to its continuum. The RAGE simulations were performed with 50 000 - 200 000 zones and 2 - 5 levels of AMR refinement. More details on the physics and setup of the models can be found in their respective papers, cited above.

2.2 AB Magnitudes

SN light curves are usually characterized by a brief, intense pulse associated with shock breakout from the surface of the star followed by either a steep or gradual decline as the fireball expands and cools. The light curve may rebrighten at later times if the explosion creates large masses of ^{56}Ni , whose decay photons diffuse out of the ejecta on timescales of weeks to months. To compute AB magnitudes for a SN in a specific filter we first cosmologically redshift and dim its rest-frame spectrum, $F'(\lambda)$:

$$F(\lambda) = \frac{F' \left(\frac{\lambda}{1+z} \right)}{(1+z)4\pi d_L^2(z)}. \quad (1)$$

Here, $d_L(z)$ is the luminosity distance:

$$d_L(z) = (1+z)c/H_0 \int_0^z \frac{1}{\sqrt{\Omega_M(1+z)^3 + \Omega_\Lambda}} dz. \quad (2)$$

AB magnitudes, m_{AB} , in specific filters are then computed from

$$m_{\text{AB}} = -2.5 \log_{10} \left(\frac{\int_0^\infty F(\lambda) T(\lambda) d\lambda}{\int_0^\infty F_0(\lambda) T(\lambda) d\lambda} \right), \quad (3)$$

where $T(\lambda)$ is the filter transmission function and $F_0(\lambda) = 3.630781 \times 10^{-20} c \lambda^{-2}$ ergs $\text{cm}^{-2} \text{s}^{-1}$, the reference spectrum for AB magnitudes.

Radiation blueward of $\lambda_{\text{Ly}\alpha} = 1216 \text{ \AA}$ emitted at $z > 6$ may be redshifted into $\lambda_{\text{Ly}\alpha}$, be resonantly scattered, and never be observed (Gunn & Peterson 1965). Consequently, at $z > 6$ we simply take all SN flux shorter than $\lambda_{\text{Ly}\alpha}$ to be absorbed by the IGM and remove it from the spectrum. After reionization, there still exist clouds of neutral hydrogen so some flux blueward of $\lambda_{\text{Ly}\alpha}$ from events at $z < 6$ may still be absorbed. To account for this partial absorption in our spectra we use the model in Madau (1995).

2.3 Cosmic SFRs/SNRs

Cosmic SNRs depend directly on global SFRs and their mass functions. SFRs derived from semianalytical models (e.g., Wise & Abel 2005; Weinmann & Lilly 2005) and numerical simulations over the years have varied by a factor of 200 or more depending on redshift (see, e.g., Figure 5 of Whalen et al. 2013a). More recently, simulations using older cosmological parameters have also produced SFRs that are not

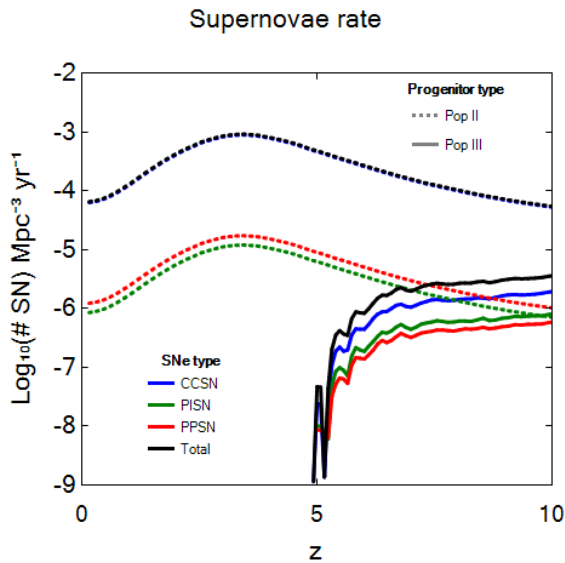


Figure 1. Pop III (solid) and Pop II (dashed) SNRs as a function of redshift, including CC (blue), PI (green), RPI plus PPI (red) and total (black) SNRs. The Pop II CC SNRs are essentially indistinguishable from the total Pop II rates.

consistent with current constraints on the optical depth to Thomson scattering by free electrons at high z (τ_e ; [Visbal et al. 2015](#)). To avoid these difficulties we compute Pop II SNRs from cosmic SFRs extrapolated from observations of GRBs, which are used as tracers of early SF ([Robertson & Ellis 2012](#)). We apply the Salpeter IMF ([Salpeter 1955](#)) to convert these rates to SNRs, adopting the lower limits to the GRB rates to be conservative.

Pop III SNRs were calculated with a semi-analytical model that utilises a cosmologically representative set of halo merger trees with detailed prescriptions for radiative and chemical feedback on star formation in the halos ([Hartwig et al. 2015](#); [Magg et al. 2016](#)). This model assumes a logarithmically flat IMF ([Greif et al. 2011](#)) for Pop III stars, whose masses are randomly sampled over an interval of 1 - 300 M_\odot . This IMF was chosen because it produces the full range of explosions expected for primordial stars. By tracing all the individual randomly generated Pop III stars, the model makes self-consistent predictions for SNRs over the mass range of each explosion type discussed earlier.

SNRs within each explosion type are further partitioned by progenitor masses for which there are light curves. Thus, CC SNRs are divided into the two mass bins from 15 - 30 M_\odot , RPI SNRs are partitioned across nine bins from 90 - 140 M_\odot , and PI SNRs are calculated for five bins from 150 - 250 M_\odot . We show total SNRs for each explosion type as a function of redshift in Figure 1. As expected, Pop III SN rates taper off with redshift as the universe becomes more chemically enriched, falling off dramatically at $z \sim 5$ when metals become present in most of the universe. In contrast, Pop II SNRs rise over this interval as metals contaminate more and more stars, reaching a peak at $z \sim 2 - 3$ that coincides with the observed peak in cosmic SFR due to galaxy formation.

2.4 Magnification Functions

We calculate magnification functions in wide fields due to strong lensing by both galaxy clusters and massive galaxies. These functions, or maps, predict what fraction of the sky is magnified by a factor of μ or more as a function of source redshift. Magnification maps for galaxy clusters are derived from a statistical model developed by [Maturi et al. \(2014\)](#). This model takes the lensing objects to be dark matter haloes with Navarro-Frenk-White (NFW) density profiles [Navarro et al. \(1996\)](#) with a Sheth-Tormen distribution in mass, $N(m, z)$, where N is the number density of haloes at or above a mass m at redshift z . For each redshift, the area on the sky that is magnified by a factor of μ or more is calculated by adding the contribution from every object at lower redshifts. $P_S(\mu, z_S)$, the fraction of the area in the source plane at redshift z_S with magnification greater than μ , is the optical depth of all lenses between the observer and the source:

$$P_S(\mu, z_S) = \frac{1}{4\pi D_S^2} \int_0^{z_S} \int_0^\infty N(m, z) \sigma_d(m, z, z_S) dm dz, \quad (4)$$

where D_S is the angular diameter distance to the source and

$$\sigma_d(z_S) = \eta_0^2 \int_{B_l} \frac{d^2x}{|\mu(x)|} \quad (5)$$

is the cross section of a lens with a length-to-width ratio greater than d over an area B_l in the lens plane. Here we define the dimensionless coordinates $x = \theta/\theta_0$ and $\eta_0 = (D_S/D_l)\theta$ for the lens and source planes, respectively.

We take the lenses to be distributed sparsely enough that their areas do not overlap and are thus additive. These magnification areas become less certain at low μ because NFW profiles more accurately represent lensing objects near their cores where densities are high. Our assumption that lensing areas do not overlap also breaks down at low μ , so we only compute magnification areas for $\mu \geq 2$. For $1 < \mu < 2$ we logarithmically extrapolate the area from its value at $\mu = 2$ (Section 3.3). This approach does not return the original field of view (FoV) as μ approaches 1 so our maps represent a lower limit to the area on the sky that is strongly lensed. At $\mu = 1$ we simply take the magnified area to be the FoV. At the other extreme, the magnified area falls as μ^{-2} at large μ for geometrical reasons, so at $\mu > 100$ we take it to be the area at $\mu = 100$ scaled downward by this factor.

We calculate magnification functions for massive galaxies with the ([Collett 2015](#)) model. The galaxies are assumed to be isothermal ellipsoids with velocity dispersions drawn from the observed velocity dispersion function from SDSS ([Choi et al. 2007](#)). We truncate the velocity dispersion function between 50 and 400 km s^{-1} . Like clusters, these lensing galaxies are assumed to be randomly distributed but they are taken to have a constant comoving density out to $z = 2$. We draw lens ellipticities from the velocity dispersion dependent fit of Equation 4 in [Collett \(2015\)](#) and have neglected the effect of compound lensing, which, while rare, can produce extreme magnifications of high redshift sources ([Collett & Bacon 2016](#)). The parameters for both models are listed in Table 1. The mass limits listed for the [Collett \(2015\)](#) model are the masses residing within the Einstein radius. Since the two models cover different ranges in lens mass, the total area that is magnified within the FoV can be approximated by

Table 1. Magnification Model Parameters

	Maturi	Collett
Mass distribution	Sheth-Tormen	Empirical
Density profile	NFW	Isothermal ellipsoid
Mass range	$10^{13} - 10^{15} M_{\odot}/h$	$< 10^{13} M_{\odot}$
Redshift range	$0.05 < z < 10$	$0.015 < z < 2.0$

simply summing their respective contributions. The Collett (2015) model produces magnified areas that are somewhat larger than those of Maturi et al. (2014), by up to 50%, but their overall agreement suggests that our areas are accurate to within an order of magnitude. Rather than sum the respective $P_S(\mu, z_S)$ of the two models to obtain the total area of the FoV that is lensed, we calculate the number of lensed SNe from each model separately and sum them to obtain the total number which is equivalent.

2.5 Lensed SN Detection Rates

The magnification required to detect a SN at redshift z is

$$\mu(\tau, z, F(\tau)) = \max(10^{0.4(m(\tau, z) - m_L)}, 1), \quad (6)$$

where $F(\tau)$ is the spectrum at a time τ after shock breakout in the observer frame, $m(\tau, z)$ is the AB magnitude for the SN, and m_L is the AB magnitude detection limit of the survey in the given filter. This minimum magnification is then used to compute $P_S(\mu, z_S)$ to calculate the area in the source plane with enough magnification to detect the SN. We neglect demagnification by cosmic voids (Hilbert et al. 2009; Mason et al. 2015).

The total number of lensed SNe observed in an interval Δz at z is

$$N(z, \Delta z) = \int_z^{z+\Delta z} S(z) A_{\text{FoV}} dV(z), \quad (7)$$

where A_{FoV} is the angular area covered by the survey or FoV of the telescope and

$$S(z) = \int_0^{\tau_U} P_S(\mu(\tau, z, F(\tau)), z_S) \text{SNR}(z) d\tau. \quad (8)$$

the total number of SNe in a mass range per volume (in Mpc^{-3}) that are visible at z . Here, $\text{SNR}(z)$ is the supernova rate in $\text{Mpc}^{-3} \text{yr}^{-1}$, τ_U is the upper limit in ages for which we have spectra, and the integration is performed over τ to capture SNe of all ages. We assume that τ_U is small in comparison to the cosmological time corresponding to Δz since an event visible at z actually exploded at a slightly higher z . To predict the number of lensed SNe of a particular type that would be detected, $N(z, \Delta z)$ is summed over the corresponding range in progenitor mass.

2.6 Transient Identification

$N(z, \Delta z)$ is the number of SNe that would appear in a single or stacked observation of the FoV under the assumption that their luminosities remain nearly constant over the exposure

time. But they can only be identified as SNe by subtracting two or more exposures of the same FoV, a procedure we call image pairing. Objects that appear, disappear, or change in brightness over the time between observations, or cadence $\Delta\tau$, are tagged as SN candidates. To verify that a candidate actually is a SN, follow-up observations are required. Ideally, spectroscopic measurements of distinctive emission lines could identify the transient as a SN. Alternatively, broadband follow-up observations could match the light curve to a certain SN type. To perform such followups the event must be visible after initial identification, so we discard transients disappearing between observations. Our SN detections are therefore objects that appear between exposures as well as objects that have changed brightness by more than 25%. As this is an arbitrary threshold, chosen to reflect changes in flux that can be easily detected, we considered a range of thresholds to investigate their effect on our number counts in Section 3.3.

Variable stars in our galaxy can appear as SN contaminants in image pairings unless they are known and catalogued. However, even previously unknown variable stars will only contaminate the first pairing and, after being identified as such, can be discarded from subsequent pairings. Spectroscopic follow-up could distinguish SNe from variable stars. Alternatively, new detections at the same position in later observations would likewise reveal the object to be a variable star.

2.6.1 New SNe

If $P_S(\mu, z_S)$ is the fractional area of a FoV in which a lensed SN is visible at a given stage of evolution, then $P_S(\mu, z_S) = 1$ if $m(\tau, z) < m_L$. If the fractions of the FoV in which the SN is visible in the first and second images of a pairing are $P_S(\mu_1, z_S)$ and $P_S(\mu_2, z_S)$, where μ_1 and μ_2 are the magnifications required to observe the SN in images 1 and 2 respectively, then the fractional area in which the SN appears in the pairing itself is

$$\Delta P_S(z_S) = P_S(\mu_2, z_S) - P_S(\mu_1, z_S) \text{ if } P_S(\mu_2, z_S) > P_S(\mu_1, z_S), \quad (9)$$

where $\mu_1 = \mu(\tau - \Delta\tau/(1+z))$ and $\mu_2 = \mu(\tau)$. $\Delta P_S(z_S)$ is then used in Equation 8 as $P_S(\mu(\tau, z, F(\tau)), z_S)$.

2.6.2 Evolving SN

We flag a change in flux in the FoV as a SN if it appears in consecutive images and it has increased or decreased by 25% or more. Since the candidate appears in both images the image with the smallest area with enough magnification for a detection should be used:

$$P_S(z_S) = \min(P_S(\mu_1, z_S), P_S(\mu_2, z_S)). \quad (10)$$

We also require that $|m(\tau - \Delta\tau/(1+z), z) - m(\tau, z)| \geq 2.5 \log_{10}(1.25)$, which guarantees that the brightness has changed by at least 25% or more. As in Equation 9, $\mu_1 = \mu(\tau - \Delta\tau/(1+z))$ and $\mu_2 = \mu(\tau)$. $P_S(z_S)$ is then used in Equation 8.

2.6.3 Multiple Flaggings of the Same SN

In principle, a SN can explode, fade below m_L , and then later rebrighten and become observable again. Such events could

be mistakenly flagged as new SNe twice in different image-pairings. When considering the area in which new SNe are detected in consecutive exposures, all SNe that have already been observed should be discarded. $P_S(\mu_1, z_S)$ must therefore be replaced by the largest $P_S(\mu, z_S)$ from any previous image among the consecutive images. Equation 9 becomes

$$\Delta P_S(i, z_S) = P_S(\mu_i, z_S) - \max_{k < i} (P_S(\mu_k, z_S)) \quad (11)$$

if $P_S(\mu_i, z_S) > \max_{k < i} (P_S(\mu_k, z_S))$. Each $P_S(\mu_i, z_S)$ corresponds to the fraction of the sky in which the SN can be detected in a given observation. The i label the observations, i.e., $P_S(\mu_{i+1}, z_S)$ is for an observation one cadence later. Since $P_S(\mu_i, z_S)$ is bounded there is an i_{\max} for which $P_S(\mu_i, z_S)$ is maximum. The total area $P_S(z_S)$ from all $i < i_{\max}$ is then zero. When summing over all $i < i_{\max}$ in Equation 11 we keep only the subset of i for which $P_S(\mu_i, z_S) > \max_{k < i} (P_S(\mu_k, z_S))$. This subset retains all positive results from Equation 11. We index this subset with m , and Equation 11 then becomes

$$\Delta P_S(m, z_S) = P_S(\mu_m, z_S) - P_S(\mu_{m-1}, z_S). \quad (12)$$

We sum this to obtain the fraction of the FoV in which it is possible to observe new, distinct SNe. Since before the explosion the area is 0 (i.e., $P_S(\mu_0, z_S) = 0$) there is a sum of disjoint, uninterrupted intervals from 0 to $\max(P_S(\mu_i, z_S))$ so the sum reduces to $\max(P_S(\mu_i, z_S))$. The number of SNe observed also depends on the SNR and Δt between observations, where $\Delta t < \Delta \tau$ and is preferably as small as possible. To include the entire light curve in the calculation we add an additional index n dividing $\Delta \tau$ in $N = \Delta \tau / \Delta t$ equal intervals. Equation 12 is then applied to each interval, where $\mu_i = \mu_{i,n}$ denotes the iteration within $\Delta \tau$. The total fraction of the FoV magnified above the threshold for detection multiplied by the formation time is then

$$\sum_{n=1}^N P_{S,n}(z_S) \Delta t = \sum_{n=1}^N \max(P_S(\mu_{i,n}, z_S)) \Delta t. \quad (13)$$

Since in this fraction of the FoV usually just the peak of the light curve can be seen we call it the peak area. It does not take into account the start and end of the observations. At these points there might be observations of SNe part of the way through their light curves which might give rise to detections of unique SNe even though it would have been an extra detection of an already observed SNe if conducted later in the survey. This should, however, be a small effect and if the time for the consecutive observations is significantly longer than the duration of the light curves the effect will be negligible. In multiple consecutive observations, every evolving SN has been already counted as an emergent SN at some point, and the method only counts distinct events.

3 RESULTS

We consider two LSST surveys. The first is the main survey, which covers 20000 deg² nearly a 1000 times in three filters, with the deepest exposure reaching $m_{AB} = 24.45$. The second is an alternative deep survey (ADS) whose purpose is to detect measurable numbers of Pop III SNe. It consists of two deeper exposures one year apart in 10 deg² FoVs in two filters. Each exposure is either 84h and 420h, and we vary the area while holding the exposure time constant to determine

Table 2. The brightest CC SN and PI SN in the z and y bands. Here, z is the redshift at which the SN is brightest in the given filter, m_{AB} is the peak AB magnitude of the event at this redshift, t_p is the time in the rest frame at which the SN reaches peak brightness, and μ_{\min} is the minimum magnification for the transient to be detected in the LSST main survey.

Type	CC	PI	CC	PI
Filter	z	z	y	y
M_{\star} (M_{\odot})	15	250	15	250
E_{SN} (foe)	2.4	94	2.4	94
z	5.5	5.0	5.1	5.0
t_p	0.8 d	21.2 d	5.4 d	21.2 d
m_{AB}	29.36	25.90	29.21	25.95
μ_{\min}	92	3.8	440	22

the field that would maximize the number of Pop III SN counts, as described below.

The main survey will be performed in the i , z , and y bands but the ADS is done just in the y and z bands. The i , z and y bands cover 6800–8400 Å, 8000–9350 Å and 9000–10300 Å respectively. As discussed in the Introduction, the Gunn-Peterson trough imposes upper limits on the redshift at which an event can be observed in a given filter. For the i , z , and y filters these limits are $z = 6.0$, 6.7 , and 7.5 , respectively. Table 2 shows some of the properties of the CC SN and PI SN that are brightest in the y and z bands. The CC SN is brightest in these two filters at $z = 5.5$ and 5.1 rather than at the lowest redshift $z = 5$, at which it is closest to Earth. This is due to the fact that more flux may be redshifted into a given filter from a higher z if it originates from a brighter region of the rest frame spectrum, and this can more than compensate for the greater distance to the event. The PI SN is brightest in both bands at the lowest redshift considered, $z = 5$.

We show light curves for these explosions in Figure 2 and summarize their properties in Table 2, including the upper limiting case of a Pop I CC SN that is 2–3 magnitudes brighter than a Pop III CC SN of equal energy (Section 2.1.2). None of the SNe reach the detection limit of the main survey so they would have to be strongly lensed to be observed. The PI SN is visible without lensing in the y and z bands in the ADS. Only the bright Pop I SN is visible in the ADS in the y and z bands without lensing. LSST has significantly better sensitivity in the z band, but at the cost of the redshift at which the event is visible.

3.1 Main Survey

The main survey will reach $m_{AB} = 24.0$, 24.5 and 22.6 in the i , z and y bands, respectively, for 30s exposures (LSST takes pairs of 15s exposures each night; Ivezić et al. 2008). The exposures range over 30000 deg² on the sky for an actual area of 20000 deg², which we take to be the FoV. Each location on the sky will be visited nearly 1000 times over 10 years for an average revisit every 3.6 days. Although cadences from a few days up to 10 years can be obtained with the proper

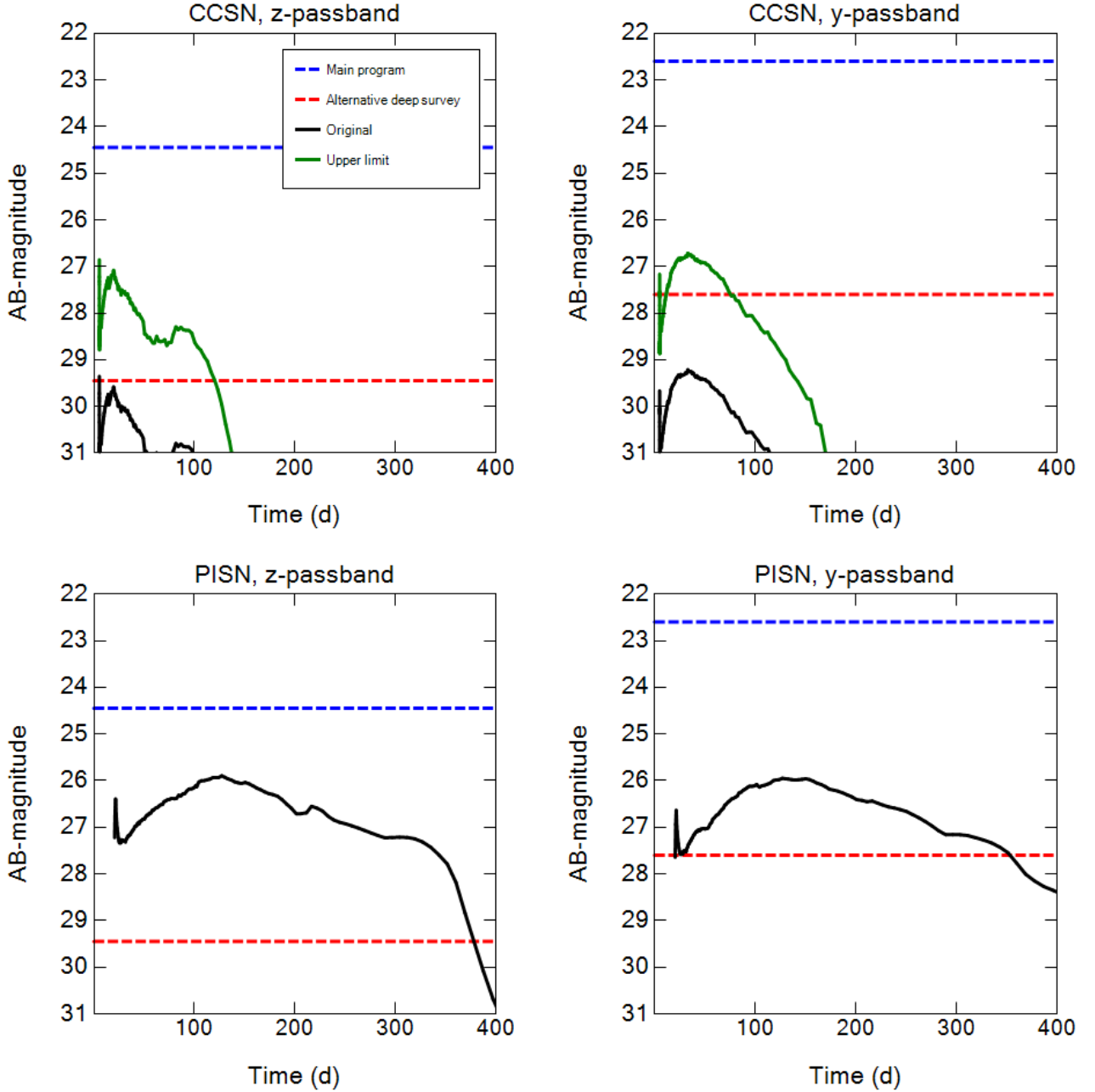


Figure 2. Light curves for the brightest CC SN (top panels) and PI SN (bottom panels) in the z and y bands at $z = 5.1$ and 5.5 , respectively. The x-axis is the time in the observer frame τ . In the upper panels the black line is the Pop III CC SN light curve and the green line is the light curve expected for a Pop I CC SN of equal energy and progenitor mass, which is brighter as discussed in Section 2.1.2. The dashed horizontal lines are the detection limits for the main survey (blue) and the ADS (red).

choice of images, we adopt 3.6 days as the cadence in our study. Number counts for new SNe are maximized by using as short a cadence as possible since some SNe might appear and then fade below the detection limit of the survey at longer cadences. Also, fewer images can be used at longer cadences unless they overlap.

As noted above, the main survey cannot detect unlensed SNe at $z \sim 5 - 7$ in the i , z , or y bands. However, as shown in

Figure 3 and Table 3, it could find large numbers of lensed Pop I/II SNe in the z -band: $\sim 17 - 1400$ CC SNe depending on their brightness, ~ 100 PP SNe and ~ 1 PPI SN. Only a tenth as many Pop I/II events will appear in the y -band, ~ 11 PI SNe, no PPI SNe, and at most ~ 110 CC SNe. Only 1 - 2 Pop III SNe will appear in any of the bands (PI SNe). These low numbers are due to the number of Pop III stars at $z < 7$, not the intrinsic brightness of their explosions.

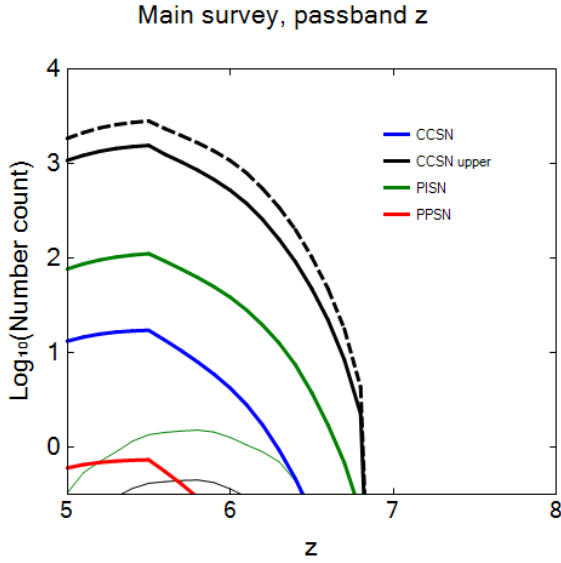


Figure 3. Number of Pop II (thick lines) and Pop III (thin lines) SNe detected per unit redshift in the main survey. These SNe are all lensed because the main survey lacks the sensitivity to detect unlensed events. The black dashed line is the predicted number of all explosions when SNe that rebrighten are not rejected as new events. The failure to properly identify such SNe can lead to number counts that are nearly twice the actual values.

It is evident from the black dashed line in Figure 3 that the failure to reject rebrightening as a spurious event can lead to number counts that are nearly twice the actual values. As noted in Section 2.6.3, variations in the light curves of some SNe can cause them to be detected, fade, and then be detected again when they brighten later, mimicking two new events if they are not properly identified. The breaks in the plots at $z \sim 5.5$ are due to Ly α beginning to be redshifted into the filter: at higher redshifts more and more of the radiation from the explosions is scattered by neutral hydrogen so detection rates fall.

3.2 ADS

Two 84h exposures in a single 10 deg^2 field one year apart in the ADS would yield a gain of five in AB magnitude over the main survey, $m_{AB} = 29.5$ and 27.6 in the z and y bands, respectively. Two 420h exposures would achieve $m_{AB} = 30.4$ and 28.5 in the z and y bands. Each ADS exposure is assumed to be a single image in our calculations. This approximation will not affect the number count of PI SNe because their light curves vary slowly over time but might affect those of CC SNe, which are dimmer and more transient. Nevertheless, at the redshifts we consider they are still extended events in comparison to the 1 - 2 night explosion peaks of most low-redshift SNe, so our approximation is valid.

We show number counts for Pop III SNe by explosion type for the simplest case in which the 84h exposures are carried out in a single 10 deg^2 field in Figure 4. About 2 unlensed PI SNe are expected from $z \sim 5 - 6.4$ in the z band. In the y band about 1 unlensed PI SN are expected from $z \sim 5 - 6$. CC SN detections are unlikely in either band, even at

Table 3. Predicted counts of lensed SNe for the main survey by filter and type.

SN Type	i	Filter	
		z	y
Pop II CC (hi)	130	1400	70
Pop II CC (lo)	0	17	0
Pop II PI	11	110	3.6
Pop II II n	0	5	0
Pop II PPI	0	0.74	0
Pop III CC (hi)	0	0	0
Pop III CC (lo)	0	0	0
Pop III PI	0	1.5	0
Pop III II n	0	0	0
Pop III PPI	0	0	0

their upper limit in brightness, so none will be found at their nominal brightness. The PI SNe that appear in this survey are all of $150 - 250 M_{\odot}$ RSGs. These numbers can be partly understood from Figure 2. Even with the deeper exposure of the ADS, the unlensed CC SN is only visible for a short time in the z band, and it is much less likely to be lensed because the FoV is so small in comparison to the main survey. On the other hand, PI SNe are visible for much longer times so the ADS will detect several of them in spite of its small FoV. Like CC SNe, they will not be lensed because only a fraction of the already small FoV will be magnified. We do not consider 420h exposures in a single 10 deg^2 field because they are so long (~ 50 nights) that variability of the light curves would distort our counts.

84h is the minimum exposure required to find at least one Pop III SN in a single 10 deg^2 field. But we can also estimate the maximum number of Pop III SNe that could be found by partitioning the 84h and 420h exposures across different areas on the sky to obtain a larger FoV. The trade-off of the larger FoV is the lower sensitivity of any single exposure. We show Pop III SN number counts from $z \sim 5 - 7$ for both exposures as a function of FoV and its AB magnitude limit in Figure 5, assuming a cadence of one year. These numbers peak at ~ 8 with the 84h exposures at a FoV of 250 deg^2 and $m_{AB} = 27.6$. PI SNe dominate these counts, ~ 7 versus ~ 1 CC SN.

We also show PI SN counts by progenitor mass, all of which are RSGs because the BSG explosions are too faint to be seen. The $250 M_{\odot}$ PI SNe will be most numerous (~ 3) but ~ 4 of them will be $150 - 200 M_{\odot}$ PI SNe and ~ 1 will be a CC SN. The number of $250 M_{\odot}$ PI SNe increases with FoV, completely dominating the number count above 1000 deg^2 . Number counts increase by roughly a factor of five with the 420h exposures, with a broader maximum at $\sim 1000 - 2000 \text{ deg}^2$. The number of $250 M_{\odot}$ PI SNe rises relatively slowly and eventually dominates the number count but then begins to fall above $\sim 6000 \text{ deg}^2$. The number of Pop III SNe in the y filter is greatest in the 10 deg^2 FoV for the 84h exposures. But with at most one predicted detection, prospects for finding Pop III SNe in this filter are bleak and

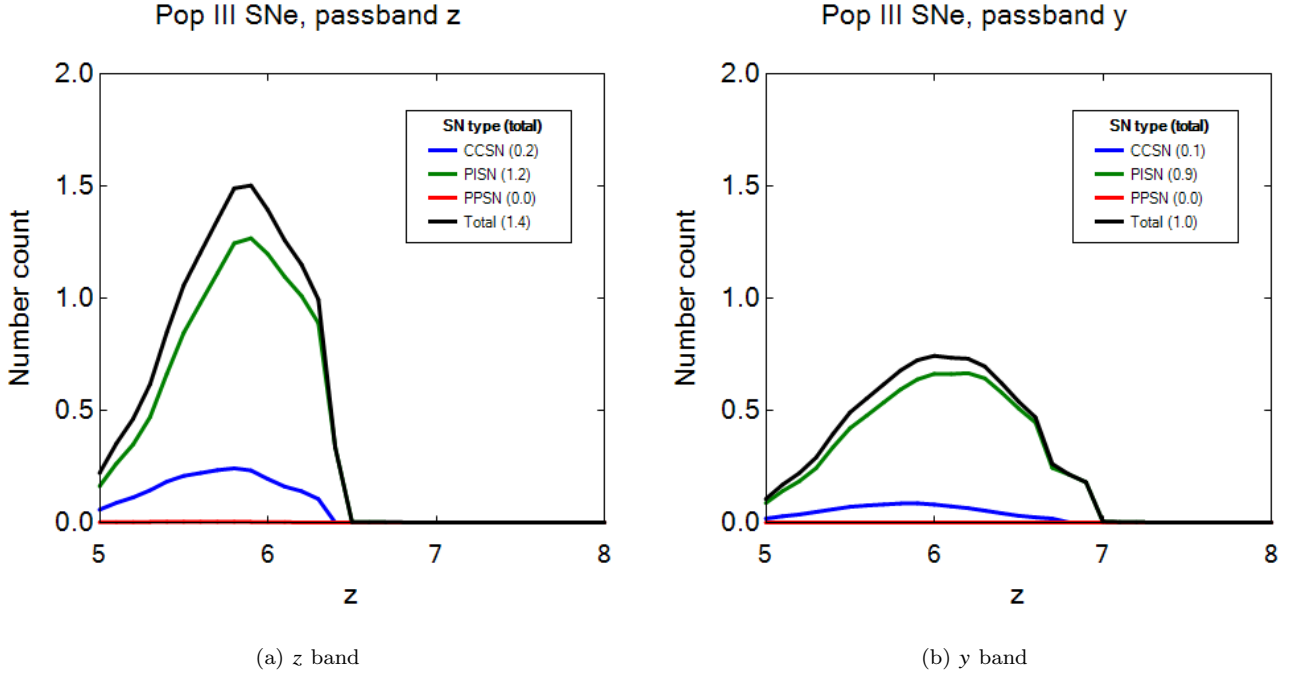


Figure 4. Pop III SN number counts in the z and y bands for two 84h exposures in a single 10 deg^2 FoV one year apart in the ADS. These are unlensed events because of the low probability of lensing in the relatively small FoV. The most likely detections are of PI SNe at $z < 6.4$. It is unlikely that any Pop III CC SNe will be detected. On average about one SN is expected to be found at $z \sim 6$ in either filter.

are not included in Figure 5 (but about 5 could appear in the 420h exposures).

3.3 Sources of Uncertainty

The primary source of uncertainty in our SN number counts is the rest frame SNRs, which are derived from cosmic SFRs and the assumed IMF. The global SFRs inferred from GRB observations by Robertson & Ellis (2012) vary by $\sim 20\%$ at $z = 5$ to a factor of 2–3 at $z = 7$. Since our SN number counts are directly proportional to the SFRs they vary by the same factor in this parameter. We adopted a Salpeter IMF for the Pop II/I stars in our models to obtain conservative counts. If we instead use the more realistic Kroupa IMF we obtain counts that are $\sim 50\%$ higher. There is a large uncertainty in the IMF of Pop III stars but SN counts in the main survey are dominated by Pop II/I explosions so this uncertainty does not impact the total counts. The ADS is much more sensitive to uncertainties in the Pop III IMF.

3.3.1 SN Type

Since at most 1% of CC SNe are Type II_{ne}, and only five Pop II but no Pop III II_{ne} would be found in the main survey, the actual fraction of CC SNe we take to be Type II_n has little impact on our rates. Less than one PPI or RPI SNe will be observed, so the number of $107.5 - 112.5 M_{\odot}$ stars we take to die as PPI events rather than RPI SNe would not change our counts. We find in general that only RSG CC and PI SNe will be observed, except at the upper limit of brightness

taken for CC events in which a few energetic $15 M_{\odot}$ BSG progenitor explosions could be found. Our predicted number counts are therefore linearly dependent on the fraction of stars that die as RSGs (75% in our study). Below we discuss each survey concerning CC SN and PI SN.

At the lower limit of CC SN luminosity only the most energetic $15 M_{\odot}$ explosions contribute to the number count in the main survey. At the upper limit, all $15 M_{\odot}$ RSG, the more energetic $15 M_{\odot}$ BSG, and the more energetic $25 M_{\odot}$ RSG SNe contribute. Thus, the SN counts have some dependence on the fractions assumed to be 0.6, 1.2 or 2.4 for (which are equal in our study). RSG PI SNe of all masses contribute to our number counts. These points are also true of the ADS except that the most energetic $15 M_{\odot}$ RSG explosions contribute almost all the number count.

3.3.2 Detection Criteria

In our detection criteria we flag every object whose flux has changed by 25% or more as a SN. Changing this threshold has no effect on the predicted numbers of SNe in the main survey because it only tallies new events because the area on the sky being surveyed never changes. Any new detection at the site of a previous one due to a change in its light curve is simply discarded, with no effect on the count. However, the ADS counts evolving sources as new SNe and is therefore sensitive to the threshold. But this effect is small. We find that changing the threshold from 25% to 1% only increases the number count by ~ 0.01 .

There is a dependence of number count on the cadence, and it can be used to set the actual cadence. Although the

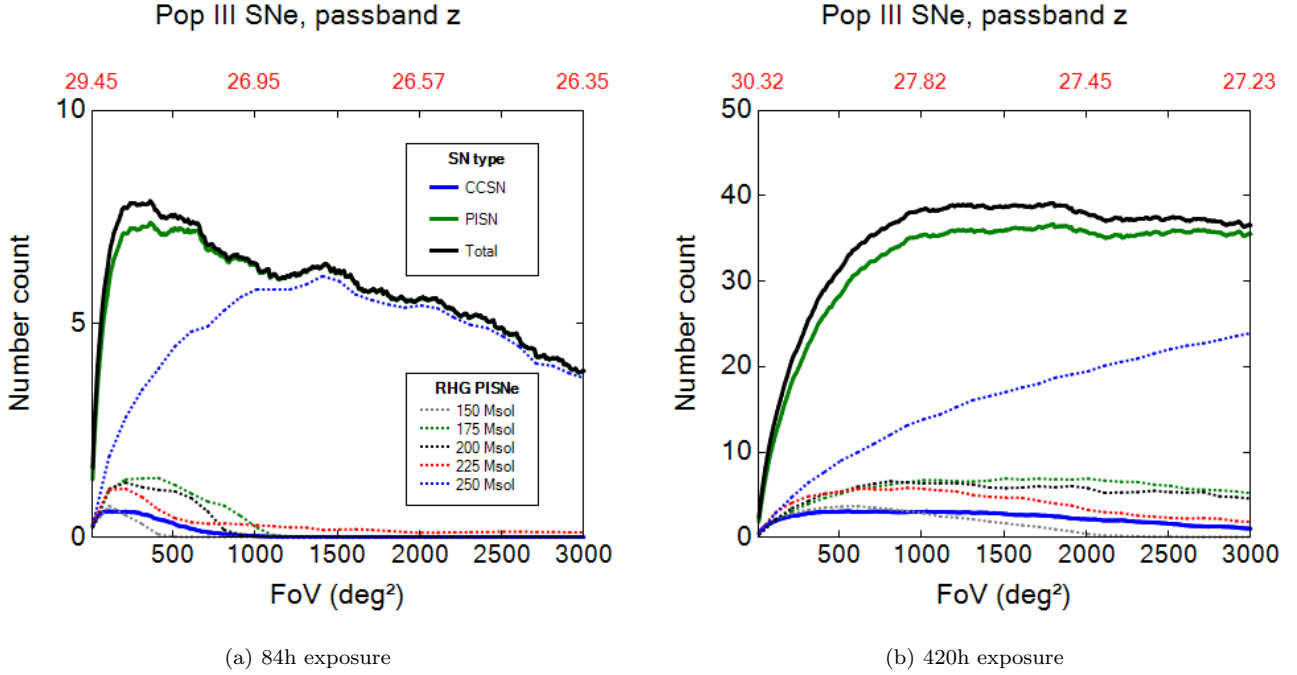


Figure 5. Pop III SN number counts in the z band in the ADS as a function of FoV and sensitivity for the given exposures. Left panel: 84h; right panel: 420h. The lower x-axis is FoV in deg^2 and the upper x-axis is the corresponding AB mag limit in red. The CC SN number counts shown are for their upper brightness limits.

cadence of the main survey is already fixed at 3.6d on average, number counts in the ADS increase until the cadence reaches a few times 10 days and are more or less flat thereafter. Consequently, number counts in the ADS are not sensitive to cadence above 1 - 2 months.

3.3.3 Scattering / Absorption

We treat attenuation of flux due to $\text{Ly}\alpha$ scattering with the model of Madau (1995) at $z < 6$ and with Gunn & Peterson (1965) for $z > 6$. The errors in Madau (1995) can be large but $\lambda_{\text{Ly}\alpha}$ is only redshifted through the i band and $\sim 35\%$ of the z band at $z < 6$. The large uncertainties in Madau (1995) therefore have little impact on our results because of the low numbers of counts in the i band and because they only affect part of the z band. High-redshift SNe might be obscured by dust at lower galactic altitudes. This will likely reduce the number of detections somewhat because LSST covers most of the sky and the disk of the Milky Way cuts through it. There may also be extinction in the host galaxies. This extinction depends on the metallicity. Pop III galaxies are believed to be free of dust, so they would not obscure explosions (Rydberg et al. 2017). Dust in the host galaxies of Pop II SNe may dim them but the extinction is expected to be weak because they are being observed in rest-frame UV. At $z \sim 5 - 7$ the host galaxies also likely have low metallicities and less dust.

3.3.4 Lensing Model

A source of potentially high uncertainty in our lensing models is the fraction of the sky with $1 < \mu < 2$ (Section 2.4). The interpolation we use yields a rather severe lower limit because at $\mu = 1$ it returns a lensed area that is just a few percent of the sky. As a simple test of how robust our counts are with respect to this interpolation we have done it with a second-degree polynomial in the $\log_{10} - \log_{10}$ plane as well. As constraints we use $f(\mu = 1) = 1$ and $f(\mu = 2) = f_2$, where $f(\mu)$ is the fraction of the sky magnified by at least μ . The slope of the interpolation between $\mu = 2$ and $\mu = 3$ is set equal to the derivative of the polynomial.

None of the counts in the main survey change because detections there always require magnifications greater than 2, as seen in Table 2. This is true even for CC SNe at their upper limit in brightness, which are not listed in Table 2 but whose minimum magnifications can be obtained from those in the table by dividing them by ten. In the ADS the use of this interpolation adds on average only one lensed SN. Although this interpolation is arbitrary, it demonstrates the sensitivity of the counts to the magnification model at $1 < \mu < 2$.

Multiple images of SNe behind galaxies and galaxy clusters can confuse SN number counts. The appearance of such images can be separated by weeks because of time delays due to lensing, and because they appear in different regions of the sky they could be mistaken for distinct events. But unlensed explosions do not exhibit multiple images so this phenomenon will have no effect on their number counts. Time delays could boost detections of lensed explosions, but we neglect them because their numbers are expected to be small

at low magnifications and because the number of counts that require high magnification are low, so even a relatively large boost would not change them much.

4 CONCLUSION

We find that the LSST main survey will on average detect 1 - 2 Pop III SNe at $z \sim 5 - 7$ but many Pop II SNe over these redshifts: ~ 110 PI SNe and $\sim 20 - 1400$ CC SNe. All these events would be lensed because the main survey lacks the sensitivity required to detect even unlensed PI SNe. The relative numbers of Pop III and II PI SNe are due to the numbers of pristine and chemically enriched stars at these redshifts. The large range of Pop II CC SNe is due to the highly nonlinear dependence of number count on threshold magnification required to detect the event. The factor of 10 by which CC SNe are likely to vary in luminosity lead to a factor of 100 in number count. Each Pop III and Pop II SN will be flagged on average twice due to variations in their light curves. With a deeper exposure (84h) and a 300 deg^2 FoV corresponding to an observational limit of $m_{AB} = 27.6$, the ADS could discover ~ 7 Pop III PI SNe and ~ 1 Pop III CC SN. If this exposure was extended to 420h as many as ~ 35 Pop III PI SNe and ~ 5 Pop III CC SNe could be found.

Because the y and z bands limit detections to $z \sim 5 - 7$, LSST will not find Pop III SNe at cosmic dawn, $z \sim 20$. But it could probe cosmic SFRs in early galaxies and even detect explosions of a few primordial stars at the era of reionization. At present, it is not known how to distinguish Pop III SNe from Pop II SNe at lower redshifts because Pop III explosion spectra could be contaminated by lines due to metals in their vicinity. The likelihood that a given explosion is a Pop III SN rises with redshift but becomes unambiguous only at $z \sim 20 - 25$, when there has not been sufficient time to pollute the cosmos with metals.

In the long term, observations by JWST and the ELTs at $2 - 5 \mu\text{m}$ will be required to find the first SNe in the universe. But wide-field surveys in the H band by *Euclid* and the *Wide Field Infrared Survey Telescope (WFIRST)* could extend detections of lensed SNe to $z \sim 12 - 13$ in the interim and probe the properties of stars in the earliest galaxies. Calculations of lensed SN rates for these two missions at this era are now under development.

ACKNOWLEDGMENTS

We thank Daniel Holz and Matthias Bartelmann for their advice over the course of this project. CER was supported by the European Research Council under the European Community's Seventh Framework Programme (FP7/2007 - 2013) via the ERC Advanced Grant "STARLIGHT: Formation of the First Stars" (project number 339177). DJW was supported by STFC New Applicant Grant ST/P000509/1. TC was funded by a University of Portsmouth Dennis Sciama Fellowship. Maturi and MC were partially supported by the Transregional Collaborative Research Centre TRR 33.

REFERENCES

- Abel T., Wise J. H., Bryan G. L., 2007, *ApJ*, **659**, L87
 Alvarez M. A., Bromm V., Shapiro P. R., 2006, *ApJ*, **639**, 621
 Alvarez M. A., Wise J. H., Abel T., 2009, *ApJ*, **701**, L133
 Amanullah R., et al., 2011, *ApJ*, **742**, L7
 Baraffe I., Heger A., Woosley S. E., 2001, *ApJ*, **550**, 890
 Barkat Z., Rakavy G., Sack N., 1967, *Physical Review Letters*, **18**, 379
 Bradley L. D., et al., 2014, *ApJ*, **792**, 76
 Bromm V., Loeb A., 2006, in Holt S. S., Gehrels N., Nousek J. A., eds, American Institute of Physics Conference Series Vol. 836, Gamma-Ray Bursts in the Swift Era. pp 503–512 ([arXiv:astro-ph/0601216](https://arxiv.org/abs/astro-ph/0601216))
 Bromm V., Yoshida N., 2011, *ARA&A*, **49**, 373
 Bromm V., Yoshida N., Hernquist L., 2003, *ApJ*, **596**, L135
 Bromm V., Yoshida N., Hernquist L., McKee C. F., 2009, *Nature*, **459**, 49
 Chatzopoulos E., Wheeler J. C., 2012a, *ApJ*, **748**, 42
 Chatzopoulos E., Wheeler J. C., 2012b, *ApJ*, **760**, 154
 Chatzopoulos E., Wheeler J. C., Couch S. M., 2013, *ApJ*, **776**, 129
 Chatzopoulos E., van Rossum D. R., Craig W. J., Whalen D. J., Smidt J., Wiggins B., 2015, *ApJ*, **799**, 18
 Chen K.-J., Heger A., Woosley S., Almgren A., Whalen D. J., Johnson J. L., 2014a, *ApJ*, **790**, 162
 Chen K.-J., Woosley S., Heger A., Almgren A., Whalen D. J., 2014b, *ApJ*, **792**, 28
 Chen K.-J., Heger A., Woosley S., Almgren A., Whalen D. J., 2014c, *ApJ*, **792**, 44
 Chen K.-J., Heger A., Whalen D. J., Moriya T. J., Bromm V., Woosley S. E., 2017a, *MNRAS*, **467**, 4731
 Chen K.-J., Whalen D. J., Wollenberg K. M. J., Glover S. C. O., Klessen R. S., 2017b, *ApJ*, **844**, 111
 Chieffi A., Limongi M., 2004, *ApJ*, **608**, 405
 Choi Y.-Y., Park C., Vogeley M. S., 2007, *ApJ*, **658**, 884
 Coe D., et al., 2013, *ApJ*, **762**, 32
 Collett T. E., 2015, *ApJ*, **811**, 20
 Collett T. E., Bacon D. J., 2016, *MNRAS*, **456**, 2210
 Cooke J., et al., 2012, *Nature*, **491**, 228
 Dessart L., Waldman R., Livne E., Hillier D. J., Blondin S., 2013, *MNRAS*, **428**, 3227
 Eggenberger P., Meynet G., Maeder A., Hirschi R., Charbonnel C., Talon S., Ekström S., 2008, *Ap&SS*, **316**, 43
 Ekström S., Meynet G., Chiappini C., Hirschi R., Maeder A., 2008, *A&A*, **489**, 685
 Foxley-Marrable M., Collett T. E., Vernardos G., Goldstein D. A., Bacon D., 2018, preprint, ([arXiv:1802.07738](https://arxiv.org/abs/1802.07738))
 Frey L. H., Even W., Whalen D. J., Fryer C. L., Hungerford A. L., Fontes C. J., Colgan J., 2013, *ApJS*, **204**, 16
 Fumagalli M., O'Meara J. M., Prochaska J. X., 2011, *Science*, **334**, 1245
 Gardner J. P., et al., 2006, *Space Sci. Rev.*, **123**, 485
 Gittings M., et al., 2008, *Computational Science and Discovery*, **1**, 015005
 Glover S., 2013, in Wiklind T., Mobasher B., Bromm V., eds, Astrophysics and Space Science Library Vol. 396, Astrophysics and Space Science Library. p. 103 ([arXiv:1209.2509](https://arxiv.org/abs/1209.2509)), [doi:10.1007/978-3-642-32362-1_3](https://doi.org/10.1007/978-3-642-32362-1_3)
 Goldstein D. A., Nugent P. E., 2017, *ApJ*, **834**, L5
 Gou L. J., Mészáros P., Abel T., Zhang B., 2004, *ApJ*, **604**, 508
 Greif T. H., Johnson J. L., Bromm V., Klessen R. S., 2007, *ApJ*, **670**, 1
 Greif T. H., Glover S. C. O., Bromm V., Klessen R. S., 2010, *ApJ*, **716**, 510
 Greif T. H., Springel V., White S. D. M., Glover S. C. O., Clark P. C., Smith R. J., Klessen R. S., Bromm V., 2011, *ApJ*, **737**, 75

- Gunn J. E., Peterson B. A., 1965, *ApJ*, **142**, 1633
- Haemmerlé L., Eggenberger P., Meynet G., Maeder A., Charbonnel C., 2013, *A&A*, **557**, A112
- Haemmerlé L., Eggenberger P., Meynet G., Maeder A., Charbonnel C., 2016, *A&A*, **585**, A65
- Haemmerlé L., Woods T. E., Klessen R. S., Heger A., Whalen D. J., 2018a, *MNRAS*, **474**, 2757
- Haemmerlé L., Woods T. E., Klessen R. S., Heger A., Whalen D. J., 2018b, *ApJ*, **853**, L3
- Hartwig T., Bromm V., Klessen R. S., Glover S. C. O., 2015, *MNRAS*, **447**, 3892
- Hartwig T., Bromm V., Loeb A., 2017, arXiv:1711.05742,
- Hartwig T., et al., 2018, preprint, (arXiv:1801.05044)
- Heger A., Woosley S. E., 2002, *ApJ*, **567**, 532
- Hilbert S., Hartlap J., White S. D. M., Schneider P., 2009, *A&A*, **499**, 31
- Hosokawa T., Yorke H. W., Inayoshi K., Omukai K., Yoshida N., 2013, *ApJ*, **778**, 178
- Hummel J. A., Pawlik A. H., Milosavljević M., Bromm V., 2012, *ApJ*, **755**, 72
- Ivezic Z., et al., 2008, arXiv:0805.2366,
- Jeon M., Pawlik A. H., Greif T. H., Glover S. C. O., Bromm V., Milosavljević M., Klessen R. S., 2012, *ApJ*, **754**, 34
- Jerkstrand A., Smartt S. J., Heger A., 2016, *MNRAS*, **455**, 3207
- Joggerst C. C., Whalen D. J., 2011, *ApJ*, **728**, 129
- Joggerst C. C., Almgren A., Bell J., Heger A., Whalen D., Woosley S. E., 2010, *ApJ*, **709**, 11
- Johnson J. L., Greif T. H., Bromm V., Klessen R. S., Ippolito J., 2009, *MNRAS*, **399**, 37
- Johnson J. L., Whalen D. J., Fryer C. L., Li H., 2012, *ApJ*, **750**, 66
- Johnson J. L., Whalen D. J., Li H., Holz D. E., 2013a, *ApJ*, **771**, 116
- Johnson J. L., Whalen D. J., Even W., Fryer C. L., Heger A., Smidt J., Chen K.-J., 2013b, *ApJ*, **775**, 107
- Johnson J. L., Whalen D. J., Agarwal B., Paardekooper J.-P., Khochfar S., 2014, *MNRAS*, **445**, 686
- Kasen D., Woosley S. E., 2009, *ApJ*, **703**, 2205
- Kasen D., Woosley S. E., Heger A., 2011, *ApJ*, **734**, 102
- Kelly P. L., et al., 2014, arXiv:1411.6009,
- Kitayama T., Yoshida N., 2005, *ApJ*, **630**, 675
- Kitayama T., Yoshida N., Susa H., Umemura M., 2004, *ApJ*, **613**, 631
- Kozyreva A., Blinnikov S., Langer N., Yoon S.-C., 2014a, *A&A*, **565**, A70
- Kozyreva A., Yoon S.-C., Langer N., 2014b, *A&A*, **566**, A146
- Kudritzki R., 2000, in A. Weiss, T. G. Abel, & V. Hill ed., *The First Stars*. pp 127–+, doi:10.1007/10719504_21
- Langer N., Norman C. A., de Koter A., Vink J. S., Cantiello M., Yoon S.-C., 2007, *A&A*, **475**, L19
- Laureijs R., et al., 2011, arXiv:1110.3193,
- Mackey J., Bromm V., Hernquist L., 2003, *ApJ*, **586**, 1
- Madau P., 1995, *ApJ*, **441**, 18
- Magee N. H., et al., 1995, in S. J. Adelman & W. L. Wiese ed., *Astronomical Society of the Pacific Conference Series* Vol. 78, *Astrophysical Applications of Powerful New Databases*. p. 51
- Magg M., Hartwig T., Glover S. C. O., Klessen R. S., Whalen D. J., 2016, *MNRAS*, **462**, 3591
- Mason C. A., et al., 2015, *ApJ*, **805**, 79
- Maturi M., Mizera S., Seidel G., 2014, *A&A*, **567**, A111
- Mesler R. A., Whalen D. J., Lloyd-Ronning N. M., Fryer C. L., Pihlström Y. M., 2012, *ApJ*, **757**, 117
- Mesler R. A., Whalen D. J., Smidt J., Fryer C. L., Lloyd-Ronning N. M., Pihlström Y. M., 2014, *ApJ*, **787**, 91
- Montero P. J., Janka H.-T., Müller E., 2012, *ApJ*, **749**, 37
- Moriya T., Yoshida N., Tominaga N., Blinnikov S. I., Maeda K., Tanaka M., Nomoto K., 2010, in D. J. Whalen, V. Bromm, & N. Yoshida ed., *American Institute of Physics Conference Series* Vol. 1294, *American Institute of Physics Conference Series*. pp 268–269, doi:10.1063/1.3518871
- Muratov A. L., Gnedin O. Y., Gnedin N. Y., Zemp M., 2013, *ApJ*, **773**, 19
- Navarro J. F., Frenk C. S., White S. D. M., 1996, *ApJ*, **462**, 563
- Nomoto K., Tanaka M., Tominaga N., Maeda K., 2010, *New Astronomy Reviews*, **54**, 191
- O’Shea B. W., Abel T., Whalen D., Norman M. L., 2005, *ApJ*, **628**, L5
- O’Shea B. W., Wise J. H., Xu H., Norman M. L., 2015, *ApJ*, **807**, L12
- Oguri M., Marshall P. J., 2010, *MNRAS*, **405**, 2579
- Pan T., Kasen D., Loeb A., 2012, *MNRAS*, **422**, 2701
- Pawlik A. H., Milosavljević M., Bromm V., 2011, *ApJ*, **731**, 54
- Pawlik A. H., Milosavljević M., Bromm V., 2013, *ApJ*, **767**, 59
- Planck Collaboration et al., 2014, *A&A*, **571**, A16
- Planck Collaboration et al., 2016, *A&A*, **594**, A13
- Rakavy G., Shaviv G., 1967, *ApJ*, **148**, 803
- Ritter J. S., Safrank-Shrader C., Milosavljević M., Bromm V., 2016, *MNRAS*, **463**, 3354
- Robertson B. E., Ellis R. S., 2012, *ApJ*, **744**, 95
- Rydberg C.-E., Zackrisson E., Lundqvist P., Scott P., 2013, *MNRAS*, **429**, 3658
- Rydberg C.-E., et al., 2015, *ApJ*, **804**, 13
- Rydberg C.-E., et al., 2017, *MNRAS*, **467**, 768
- Safrank-Shrader C., Milosavljević M., Bromm V., 2014, *MNRAS*, **438**, 1669
- Salpeter E. E., 1955, *ApJ*, **121**, 161
- Schmidt K. B., et al., 2014, *ApJ*, **782**, L36
- Sluder A., Ritter J. S., Safrank-Shrader C., Milosavljević M., Bromm V., 2016, *MNRAS*, **456**, L140
- Smidt J., Whalen D. J., Chatzopoulos E., Wiggins B., Chen K.-J., Kozyreva A., Even W., 2015, *ApJ*, **805**, 44
- Smidt J., Whalen D. J., Johnson J. L., Li H., 2017, arXiv:1703.00449,
- Smith B. D., Sigurdsson S., 2007, *ApJ*, **661**, L5
- Smith B. D., Turk M. J., Sigurdsson S., O’Shea B. W., Norman M. L., 2009, *ApJ*, **691**, 441
- Smith B. D., Wise J. H., O’Shea B. W., Norman M. L., Khochfar S., 2015, *MNRAS*, **452**, 2822
- Spergel D., et al., 2015, arXiv:1503.03757,
- Susa H., Umemura M., 2006, *ApJ*, **645**, L93
- Susa H., Umemura M., Hasegawa K., 2009, *ApJ*, **702**, 480
- Tanaka M., Moriya T. J., Yoshida N., Nomoto K., 2012, *MNRAS*, **422**, 2675
- Tanaka M., Moriya T. J., Yoshida N., 2013, *MNRAS*, **435**, 2483
- Tominaga N., Morokuma T., Blinnikov S. I., Baklanov P., Sorokina E. I., Nomoto K., 2011, *ApJS*, **193**, 20
- Trenti M., Stiavelli M., Michael Shull J., 2009, *ApJ*, **700**, 1672
- Tumlinson J., Giroux M. L., Shull J. M., 2001, *ApJ*, **550**, L1
- Umeda H., Hosokawa T., Omukai K., Yoshida N., 2016, *ApJ*, **830**, L34
- Vanzella E., et al., 2014, *ApJL*, **783**, L12
- Vink J. S., de Koter A., Lamers H. J. G. L. M., 2001, *A&A*, **369**, 574
- Visbal E., Haiman Z., Bryan G. L., 2015, *MNRAS*, **453**, 4456
- Weaver T. A., Zimmerman G. B., Woosley S. E., 1978, *ApJ*, **225**, 1021
- Weinmann S. M., Lilly S. J., 2005, *ApJ*, **624**, 526
- Whalen D. J., 2013, *Acta Polytechnica*, **53**, 573
- Whalen D. J., Fryer C. L., 2012, *ApJ*, **756**, L19
- Whalen D., Abel T., Norman M. L., 2004, *ApJ*, **610**, 14
- Whalen D., O’Shea B. W., Smidt J., Norman M. L., 2008a, *ApJ*, **679**, 925
- Whalen D., van Veelen B., O’Shea B. W., Norman M. L., 2008b, *ApJ*, **682**, 49
- Whalen D., Prochaska J. X., Heger A., Tumlinson J., 2008c, *ApJ*, **682**, 1114

- Whalen D., Hueckstaedt R. M., McConkie T. O., 2010, *ApJ*, **712**, 101
- Whalen D. J., Smidt J., Johnson J. L., Holz D. E., Stiavelli M., Fryer C. L., 2013a, arXiv:1312.6330,
- Whalen D. J., Fryer C. L., Holz D. E., Heger A., Woosley S. E., Stiavelli M., Even W., Frey L. H., 2013b, *ApJ*, **762**, L6
- Whalen D. J., Joggerst C. C., Fryer C. L., Stiavelli M., Heger A., Holz D. E., 2013c, *ApJ*, **768**, 95
- Whalen D. J., et al., 2013d, *ApJ*, **768**, 195
- Whalen D. J., Johnson J. L., Smidt J., Meiksin A., Heger A., Even W., Fryer C. L., 2013e, *ApJ*, **774**, 64
- Whalen D. J., Johnson J. L., Smidt J., Heger A., Even W., Fryer C. L., 2013f, *ApJ*, **777**, 99
- Whalen D. J., et al., 2013g, *ApJ*, **777**, 110
- Whalen D. J., et al., 2013h, *ApJ*, **778**, 17
- Whalen D. J., Smidt J., Even W., Woosley S. E., Heger A., Stiavelli M., Fryer C. L., 2014a, *ApJ*, **781**, 106
- Whalen D. J., et al., 2014b, *ApJ*, **797**, 9
- Wise J. H., Abel T., 2005, *ApJ*, **629**, 615
- Wise J. H., Turk M. J., Norman M. L., Abel T., 2012, *ApJ*, **745**, 50
- Woods T. E., Heger A., Whalen D. J., Haemmerlé L., Klessen R. S., 2017, *ApJ*, **842**, L6
- Woosley S. E., Heger A., 2007, *Phys. Rep.*, **442**, 269
- Woosley S. E., Heger A., Weaver T. A., 2002, *Reviews of Modern Physics*, **74**, 1015
- Woosley S. E., Blinnikov S., Heger A., 2007, *Nature*, **450**, 390
- Xu H., Wise J. H., Norman M. L., 2013, *ApJ*, **773**, 83
- Yoon S.-C., Langer N., 2005, *A&A*, **443**, 643
- Yoon S.-C., Dierks A., Langer N., 2012, *A&A*, **542**, A113
- Zheng W., et al., 2012, *Nature*, **489**, 406
- de Souza R. S., Ishida E. E. O., Johnson J. L., Whalen D. J., Mesinger A., 2013, *MNRAS*, **436**, 1555
- de Souza R. S., Ishida E. E. O., Whalen D. J., Johnson J. L., Ferrara A., 2014, *MNRAS*, **442**, 1640

This paper has been typeset from a $\text{\TeX}/\text{\LaTeX}$ file prepared by the author.